Peter Wriggers
Tod A. Laursen
Editors

International Centre
for Mechanical Sciences

Computational Contact Mechanics

CISM Courses and Lectures, vol. 498

SpringerWienNewYork

SpringerWienNewYork

CISM COURSES AND LECTURES

The series presents lecture notes, monographs, edited works and proceedings in the field of Mechanics, Engineering, Computer Science and Applied Mathematics.
Purpose of the series is to make known in the international scientific and technical community results obtained in some of the activities organized by CISM, the International Centre for Mechanical Sciences.

INTERNATIONAL CENTRE FOR MECHANICAL SCIENCES

COURSES AND LECTURES - No. 498

COMPUTATIONAL CONTACT MECHANICS

EDITED BY

PETER WRIGGERS
UNIVERSITY OF HANNOVER, GERMANY

TOD A. LAURSEN
DUKE UNIVERSITY, DURHAM, NC, USA

SpringerWienNewYork

This volume contains 157 illustrations

Printed in Italy
SPIN 12068043

All contributions have been typeset by the authors.

ISBN 978-3-211-77297-3 SpringerWienNewYork

PREFACE

In recent years, computational contact mechanics has been a topic of intense research. The aim of this research has been to devise robust solution schemes and new discretization techniques for description of contact phenomena, which can then be applied to a much broader range of engineering analysis areas than is currently the case. Among the broad areas of emphasis have been finite deformation contact problems, consideration of higher order interpolations, special algorithms for rolling contact, and discrete element problems for large scale analysis. The main focus of this book is to convey modern techniques applied within the range of computational contact mechanics.

Topics of interest within the community are wide ranging, and include computational aspects of

- *spatial and temporal discretization techniques for contact and impact problems with small and finite deformations;*
- *investigations on the reliability of micromechanical contact models;*
- *emerging techniques for rolling contact mechanics;*
- *homogenization methods and multi-scale approaches to frictionless and frictional contact problems;*
- *solution algorithms for single- and multi-processor computing environments, enabling methods that span from multi-contact to multi-scale approaches; and*
- *numerical experiments related to soil mechanics using discontinuous deformation analysis.*

The different contributions in this book will cover the topics described above, while providing some needed background with respect to continuum mechanics and finite element methods. The focus will be a detailed treatment of the theoretical formulation of contact problems with regard to mechanics and mathematics. Furthermore, discretization schemes for two- and three-dimensional contact problems of small and large deformations will be discussed. These schemes include novel and innovative formulations for rolling contact applications relating to tire contact and noise generation of rolling tires. Solution techniques related to contact mechanics are also of interest; hence, solvers for large scale multi-contact problems will be discussed. This includes multi-scale contact related to quasistatic, dynamic, structural and granular applications. Special attention is also given to conjugate gradient algorithms and extensions. This will include domain decomposition methods for structural problems, their application to cellular materials and important homogenization techniques in micro-macro approaches to frictional

problems. Finally, a contribution will cover discrete element techniques for multi body contact analysis and their applications to industrial problems.

All contributions are of a theoretical and applied nature, suitable for graduate students of applied mathematics, mechanics, engineering and physics with interest in computer simulation of contact problems.

P. Wriggers and T. A. Laursen

CONTENTS

Emerging Spatial and Temporal Discretization Methods in Contact and Impact Mechanics

Tod A. Laursen

Computational Mechanics Laboratory
Department of Civil and Environmental Engineering
Duke University, Durham, NC 27708-0287, USA

Abstract The focus of this discussion will be the recent evolution of both spatial and temporal discretization techniques in contact and impact mechanics. With regard to spatial discretization, attention will be focused on the movement from traditional "node to surface" methodologies for description of contact interaction, to new "surface to surface" algorithms that in most cases have their motivation in the mortar method. While an anticipated result of this evolution was the increased numerical accuracy produced by integral forms of the contact constraints, it has also been seen that considerable robustness in large sliding applications results from the non-local character of the formulation. In this discussion both of these advantages of the surface to surface framework will be demonstrated, as will recent extensions that enable reliable simulation of self-contact phenomena.

When extending computational contact formulations to the transient regime, the consideration of reliable time integrators for impact phenomena is of interest. Accordingly, we examine some of the issues associated with time stepping in semidiscrete formulations of contact/impact, with particular emphasis on the energy-momentum paradigm as applied to impact mechanics. We consider a form of the energy-momentum approach which encompasses dissipative phenomena (such as inelasticity and friction), and focus on a numerical approach that allows for velocity discontinuities to be incorporated into the contact updating scheme.

1 Problem Formulation

We begin by summarizing the equations governing the contact of solids, with extensive consideration of the continuum formulation of large deformation contact as described in such early sources as Laursen and Simo (1993) and Wriggers and Miehe (1994). We will consider the unilateral contact constraints between two deformable bodies here, with potential (Coulomb) frictional contact between them also encompassed by the framework.

We define open sets $\Omega^{(i)} \subset \mathbb{R}^{n_{sd}}, i = \{1, 2\}, n_{sd} = 2$ or 3, to denote reference configurations of two bodies. They have boundaries $\partial\Omega^{(i)}$ which are individually subdivided into non-intersecting regions $\Gamma_\sigma^{(i)}$ (Neumann boundary), $\Gamma_\varphi^{(i)}$ (Dirichlet boundary), and $\Gamma_c^{(i)}$ (contact boundary), each invariant with time and satisfying

$$\Gamma_\sigma^{(i)} \cup \Gamma_\varphi^{(i)} \cup \Gamma_c^{(i)} = \partial\Omega^{(i)}. \tag{1.1}$$

Given a time interval $\mathbb{I} = [0, T]$, and appropriate spaces for admissible deformations $\boldsymbol{\varphi}_t^{(i)}$ and admissible variational functions $\overset{*}{\boldsymbol{\varphi}}{}^{(i)}$, the weak form of the dynamic contact problem can be thus expressed for each body (i):

Find $\boldsymbol{\varphi}_t^{(i)}$ such that for all $\overset{*}{\boldsymbol{\varphi}}{}^{(i)}$:

$$\left\langle (\rho_0 \dot{\boldsymbol{V}}_t - \boldsymbol{f}_t) \ , \ \overset{*}{\boldsymbol{\varphi}} \right\rangle^{(i)} + \left\langle D\boldsymbol{\varphi}_t \boldsymbol{S}_t \ , \ \mathrm{G}RAD[\overset{*}{\boldsymbol{\varphi}}] \right\rangle^{(i)} - \left\langle \bar{\boldsymbol{t}}_t \ , \overset{*}{\boldsymbol{\varphi}} \right\rangle_{\Gamma_\sigma}^{(i)} = \left\langle \boldsymbol{t}_t \ , \overset{*}{\boldsymbol{\varphi}} \right\rangle_{\Gamma_c}^{(i)} \ . \tag{1.2}$$

In (1.2) and throughout we make use of a shorthand description of integral products,

$$\int_{\Omega^{(i)}} (\bullet) \cdot (\bullet) \, d\Omega^{(i)} := \langle \bullet, \bullet \rangle^{(i)}, \quad \text{and} \quad \int_{\Gamma^{(i)}} (\bullet) \cdot (\bullet) \, d\Gamma^{(i)} := \langle \bullet, \bullet \rangle_{\Gamma^{(i)}}^{(i)}. \tag{1.3}$$

Values in (1.2) include reference density, ρ_0; local material velocities, $\boldsymbol{V}_t = \dot{\boldsymbol{\varphi}}_t$; and a representation of the second (symmetric) Piola-Kirchhoff stress, denoted $\boldsymbol{S}_t$. The contact surface tractions ($\boldsymbol{t}_t$) are subject to a set of spatial geometric constraints dependent on the unknown deformation mappings $\boldsymbol{\varphi}_t^{(i)}$.

The variational form in (1.2) is composed of integral *v*irtual work expressions. Taking the left hand side and summing over the contacting bodies i gives the total virtual work of the combined non-contact forces on the system:

$$\begin{aligned} G(\boldsymbol{\varphi}_t, \overset{*}{\boldsymbol{\varphi}}) := \sum_i^2 \Bigg[& \left\langle (\rho_0 \dot{\boldsymbol{V}}_t - \boldsymbol{f}_t) \ , \ \overset{*}{\boldsymbol{\varphi}} \right\rangle^{(i)} \\ & + \left\langle D\boldsymbol{\varphi}_t \boldsymbol{S}_t \ , \ \mathrm{G}RAD[\overset{*}{\boldsymbol{\varphi}}] \right\rangle^{(i)} - \left\langle \bar{\boldsymbol{t}}_t \ , \overset{*}{\boldsymbol{\varphi}} \right\rangle_{\Gamma_\sigma}^{(i)} \Bigg]. \end{aligned} \tag{1.4}$$

We use a standard Lagrangian description for the contact surfaces, designating the material points as $\boldsymbol{X} \in \Gamma_c^{(1)}$ and $\boldsymbol{Y} \in \Gamma_c^{(2)}$, respectively. Contact points on $\Gamma_c^{(2)}$ are often mapped[1] from $\Gamma_c^{(1)}$ through a *c*losest point projection minimization

$$\bar{\boldsymbol{Y}}(\boldsymbol{X}, t) := \arg \min_{\boldsymbol{Y} \in \Gamma_c^{(2)}} \| \boldsymbol{\varphi}_t^{(1)}(\boldsymbol{X}) - \boldsymbol{\varphi}_t^{(2)}(\boldsymbol{Y}) \| \ . \tag{1.5}$$

Summing the right hand side of (1.2) and establishing force balance ($\boldsymbol{t}^{(1)} = -\boldsymbol{t}^{(2)} := \boldsymbol{t}$) along the shared contact surface ($\Gamma_c^{(1)} = \Gamma_c^{(2)} := \Gamma_c$), yields a single integral expression for the *v*irtual work of contact:

$$G_c(\boldsymbol{\varphi}_t, \overset{*}{\boldsymbol{\varphi}}) := -\left\langle \boldsymbol{t} \ , \ [\overset{*}{\boldsymbol{\varphi}}{}^{(1)}(\boldsymbol{X}) - \overset{*}{\boldsymbol{\varphi}}{}^{(2)}(\bar{\boldsymbol{Y}}(\boldsymbol{X}, t))] \right\rangle_{\Gamma_c} \tag{1.6}$$

The contact problem is thus compactly stated in virtual work terms:

[1] Note that this means of identification of contact points will be revised when the mortar contact framework is introduced

Find $\boldsymbol{\varphi}_t^{(i)}$, subject to the contact constraints, such that for all $\overset{*}{\boldsymbol{\varphi}}{}^{(i)}$:

$$G(\boldsymbol{\varphi}_t, \overset{*}{\boldsymbol{\varphi}}) + G_c(\boldsymbol{\varphi}_t, \overset{*}{\boldsymbol{\varphi}}) = 0 \tag{1.7}$$

In defining the local contact conditions in the continuum problem, we may use (1.5) to identify a unit direction vector $\boldsymbol{\nu}$ aligned with the contact surface normal, as well as a *g*ap function g, such that

$$\boldsymbol{\varphi}_t^{(1)}(\boldsymbol{X}) - \boldsymbol{\varphi}_t^{(2)}(\bar{\boldsymbol{Y}}(\boldsymbol{X}, t)) = -g\,\boldsymbol{\nu}; \tag{1.8}$$

and adopt the convention whereby $\boldsymbol{\nu}$ is directed *o*utward of $\Omega^{(2)}$ such that the 'gap' is *n*egative ($g < 0$) for admissible (i.e. non-penetrated) deformations. Manipulation of (1.8) defines a geometric description of the gap magnitude,

$$g = -\boldsymbol{\nu} \cdot \left(\boldsymbol{\varphi}_t^{(1)}(\boldsymbol{X}) - \boldsymbol{\varphi}_t^{(2)}(\bar{\boldsymbol{Y}}(\boldsymbol{X}, t)) \right). \tag{1.9}$$

Following the approach given in Laursen and Simo (1993), we parameterize the projection contact surface ($\Gamma_c^{(2)}$) in reference variables ξ^α, ($\alpha = 1, n_{sd} - 1$), and derive $n_{sd} - 1$ spatial vectors $\boldsymbol{\tau}_\alpha$ through differentiation of (1.8) within this parameterization, maintaining the closest-point minimization (indicated with the overbar notation) such that

$$\boldsymbol{\tau}_\alpha := \boldsymbol{\varphi}_t^{(2)}{}_{,\,\alpha}\left(\bar{\xi}(\boldsymbol{X}, t)\right) . \tag{1.10}$$

The tangential vectors $\boldsymbol{\tau}_\alpha$ are orthogonal to the surface normal $\boldsymbol{\nu}$, and are not in general orthonormal. This requires consideration of the associated metric and its inverse,

$$m_{\alpha\beta} := \boldsymbol{\tau}_\alpha \cdot \boldsymbol{\tau}_\beta \qquad [m^{\alpha\beta}] = [m_{\alpha\beta}]^{-1}, \tag{1.11}$$

in order to define the dual basis,

$$\boldsymbol{\tau}^\alpha := m^{\alpha\beta}\boldsymbol{\tau}_\beta . \tag{1.12}$$

(Note that here the summation convention is implied on repeated indices.) The contact forces, $\boldsymbol{t}$, can now be decomposed in terms of normal (t_N) and tangential ($t_{T\alpha}$) components, i.e.

$$\boldsymbol{t} = t_N\,\boldsymbol{\nu} - t_{T\alpha}\boldsymbol{\tau}^\alpha \tag{1.13}$$

Variations of the important surface quantities, namely the gap function g and the projected surface parameterization $\bar{\xi}$, can be generated as directional derivatives aligned with deformation variation $\overset{*}{\boldsymbol{\varphi}}$. Consider

$$\delta g = -\boldsymbol{\nu} \cdot [\overset{*}{\boldsymbol{\varphi}}{}^{(1)}(\boldsymbol{X}) - \overset{*}{\boldsymbol{\varphi}}{}^{(2)}(\bar{\boldsymbol{Y}}(\boldsymbol{X}, t))] \tag{1.14}$$

and

$$A_{\alpha\beta}\,\delta\bar{\xi}^\alpha = \boldsymbol{\tau}_\beta \cdot [\overset{*}{\boldsymbol{\varphi}}{}^{(1)}(\boldsymbol{X}) - \overset{*}{\boldsymbol{\varphi}}{}^{(2)}(\bar{\boldsymbol{Y}}(\boldsymbol{X}, t))] + g\,\boldsymbol{\nu} \cdot [-\overset{*}{\boldsymbol{\varphi}}{}^{(2)}{}_{,\beta}\left(\bar{\boldsymbol{Y}}(\boldsymbol{X}, t)\right)] , \tag{1.15}$$

where the symmetric matrix $A_{\alpha\beta}$ and its inverse $A^{\alpha\beta}$ are defined as

$$A_{\alpha\beta} := m_{\alpha\beta} + g\,\boldsymbol{\nu}\cdot[\overset{*}{\boldsymbol{\varphi}}{}^{(2)}{}_{,\alpha\beta}\,(\bar{\boldsymbol{Y}}(\boldsymbol{X},t))] \qquad \text{and} \qquad [A^{\alpha\beta}] := [A_{\alpha\beta}]^{-1}\ . \tag{1.16}$$

Temporal derivatives (denoted with a superimposed dot) are calculated in the same manner, yielding a local description for a *g*ap rate, $v_N = \dot{g}$ and local measures of relative tangential motion, or *s*lip rates, $v_T^\alpha = \dot{\bar{\xi}}^\alpha$ in terms of material velocities $\boldsymbol{V}^{(i)} = \dot{\boldsymbol{\varphi}}_t^{(i)}$:

$$v_N = \dot{g} = -\boldsymbol{\nu}\cdot[\boldsymbol{V}^{(1)}(\boldsymbol{X}) - \boldsymbol{V}^{(2)}(\bar{\boldsymbol{Y}}(\boldsymbol{X},t))], \tag{1.17}$$

and

$$A_{\alpha\beta}\,v_T^\alpha = A_{\alpha\beta}\,\dot{\bar{\xi}}^\alpha = \boldsymbol{\tau}_\beta\cdot[\boldsymbol{V}^{(1)}(\boldsymbol{X}) - \boldsymbol{V}^{(2)}(\bar{\boldsymbol{Y}}(\boldsymbol{X},t))] + g\,\boldsymbol{\nu}\cdot[-\boldsymbol{V}^{(2)}{}_{,\beta}\,(\bar{\boldsymbol{Y}}(\boldsymbol{X},t))]\ . \tag{1.18}$$

The slip rates can then be used in the definition of a relative and frame indifferent *s*lip velocity as proposed in Laursen and Simo (1993). Although many choices of reference frame are possible for posing of the frictional conditions, here we opt for a completely spatial definition of the slip velocity through use of the *s*patial metric $m_{\alpha\beta}$. Consider the definition

$$\boldsymbol{v}_T := \ v_T^\beta\boldsymbol{\tau}_\beta \ = \ m_{\alpha\beta}v_T^\beta\boldsymbol{\tau}^\alpha\ . \tag{1.19}$$

The descriptions in (1.14) and (1.15) are now combined with the contact force decomposition (1.13) and substituted into the variational equation to restate the virtual work of contact in terms of the surface variations,

$$G_c(\boldsymbol{\varphi}_t, \overset{*}{\boldsymbol{\varphi}}) = \int_{\Gamma_c}[t_N\delta g + t_{T\alpha}\delta\bar{\xi}^\alpha]\,d\Gamma_c. \tag{1.20}$$

The equivalence of (1.6) and (1.20) rests upon a pair of *c*omplementarity conditions,

$$t_N\,g = 0 \qquad \text{and} \qquad t_{T\alpha}\,g = 0, \tag{1.21}$$

which establish that the contact force magnitudes (non-zero only during contact) and the gap functions g (negative only when *o*ut of contact) cannot be mutually non-zero in the continuum description. The dilitational components of the tangential variation (the last term in each of (1.15) and (1.16)) can thus be considered as zero over the contact surfaces, validating the virtual work description (1.20).

With the global virtual work expression established, we wish now to apply a standard set of Kuhn-Tucker conditions in terms of the kinematic geometry, first in the normal direction, which remains the same for both frictionless and frictional contact:

$$\begin{aligned} g &\le 0 \\ t_N &\ge 0 \\ t_N\,g &= 0 \\ t_N\,v_N &= 0\ . \end{aligned} \tag{1.22}$$

In the event that frictional response is to be described, the contact conditions may be generically introduced via the following well-known equations of evolution:

$$\begin{aligned} \Phi(\boldsymbol{t}_T, t_N) &:= [t_{T_\alpha} m^{\alpha\beta} t_{T_\beta}]^{1/2} - \mu t_N \leq 0, \\ m_{\alpha\beta} v_T^\beta &= \dot{\gamma} \frac{t_{T_\alpha}}{[t_{T_\beta} m^{\beta\gamma} t_{T_\gamma}]^{1/2}}, \\ \dot{\gamma} &\geq 0, \\ \dot{\gamma}\Phi &= 0 \end{aligned} \tag{1.23}$$

where μ is the coefficient of friction.

2 Traditional Node-to-Surface Formulation of Contact

In developing a finite element representation of the system we have described, one begins by considering $\boldsymbol{\varphi}^{(i)^h}$ and $\overset{*}{\boldsymbol{\varphi}}{}^{(i)^h}$, finite-dimensional counterparts of $\boldsymbol{\varphi}^{(i)}$ and $\overset{*}{\boldsymbol{\varphi}}{}^{(i)}$. In particular, $\overset{*}{\boldsymbol{\varphi}}{}^{(i)^h} \in \mathcal{V}^{(i)^h} \subset \mathcal{V}^{(i)}$, while $\boldsymbol{\varphi}^{(i)^h}$, considered to be continuous in time, satisfies the following for each time t:

$$\boldsymbol{\varphi}_t^{(i)^h} \in \mathcal{C}_t^{(i)^h} \subset \mathcal{C}_t^{(i)}, \tag{2.1}$$

where $\mathcal{C}_t^{(i)}$ and $\mathcal{V}^{(i)}$ are the space of admissible configurations at time t and the space of admissible variations, respectively. Substitution of these finite dimensional quantities into the global variational principle (1.7) gives a set of nonlinear ordinary differential equations of the form

$$\boldsymbol{M}\ddot{\boldsymbol{d}}(t) + \boldsymbol{F}^{int}(\boldsymbol{d}(t)) + \boldsymbol{F}^{c}(\boldsymbol{d}(t)) = \boldsymbol{F}^{ext}(t), \tag{2.2}$$

subject to initial conditions on $\boldsymbol{d}$ and $\dot{\boldsymbol{d}}$. In (2.2), $\boldsymbol{M}$ is the mass matrix, $\boldsymbol{F}^{int}$ is the internal force vector, $\boldsymbol{F}^{c}$ is the contact force vector, and $\boldsymbol{F}^{ext}(t)$ is the external force vector (consisting of known data). The vector $\boldsymbol{d}$ symbolically represents the solution vector, or a vector of nodal values of the motion $\boldsymbol{\varphi}^h$. The manipulations necessary to derive $\boldsymbol{M}$, $\boldsymbol{F}^{int}$, and $\boldsymbol{F}^{ext}(t)$ from the virtual works of the contacting bodies have been extensively treated in the literature and will not be examined here. In the semidiscrete approach, approximate solutions to (2.2) are found by applying temporal integration schemes, as will be discussed later. The quasistatic equivalent of (2.2) is formally obtained by omission of the inertial term $\boldsymbol{M}\ddot{\boldsymbol{d}}$.

Equation (2.2) is in general highly nonlinear, mostly because of the terms $\boldsymbol{F}^{int}(\boldsymbol{d})$ and $\boldsymbol{F}^{c}(\boldsymbol{d})$. The first of these, the internal force vector, often contains both geometric and material nonlinearities, causing it to depend in a complex manner on $\boldsymbol{d}$. The second, the contact force vector, derives from expression (1.20) and has a form which depends on the method of spatial discretization. We will focus on this topic in the remainder of this section as well as the next. First we will consider node-to-surface methods for approximation of contact interaction, and then in the next section, a more recent surface-to-surface approach will be summarized.

2.1 Contact Surface Discretization

An important attribute of the contact formulation we consider is that all development depends only on the configurations and variations evaluated on the contact surfaces $\Gamma_c^{(i)}$, and *not* on values in the interiors of the bodies. Thus, in considering the discretization leading to specification of $\boldsymbol{F}^c(\boldsymbol{d})$, only the restrictions of $\boldsymbol{\varphi}^{(i)^h}$ and $\overset{*}{\boldsymbol{\varphi}}{}^{(i)}$ to $\Gamma_c^{(i)^h}$ need to be considered. These restrictions are considered to be collections of local mappings (denoted by superscript e's), defined over individual element surfaces.

For example, $\boldsymbol{\varphi}^{(1)^{h\,e}}(\boldsymbol{\eta})$, with $\boldsymbol{\eta} \in \mathcal{A}^{(1)^e}$, is expressed as

$$\boldsymbol{\varphi}^{(1)^{h\,e}}(\boldsymbol{\eta}) = \sum_{a=1}^{n_{nes}} N_a(\boldsymbol{\eta}) \boldsymbol{d}_a^{(1)}(t) \tag{2.3}$$

where $\boldsymbol{d}_a^{(1)}(t)$ is a nodal value of $\boldsymbol{\varphi}^{(1)^h}$, and n_{nes} is the number of nodes per element surface. $N_a(\boldsymbol{\eta})$ denotes a standard Lagrangian shape function, defined on the biunit square $\mathcal{A}^{(1)^e}$ for three dimensional problems and on $\mathcal{A}^{(1)^e} = [-1, 1]$ for two dimensional problems. The interpolation of $\overset{*}{\boldsymbol{\varphi}}{}^{(1)^h}$ is similarly conceived, via

$$\overset{*}{\boldsymbol{\varphi}}{}^{(1)^{h\,e}}(\boldsymbol{\eta}) = \sum_{a=1}^{n_{nes}} N^a(\boldsymbol{\eta}) \boldsymbol{c}_a^{(1)}, \tag{2.4}$$

where $\boldsymbol{c}_a^{(1)}$, a nodal value of $\overset{*}{\boldsymbol{\varphi}}{}^{(1)^h}$, is independent of time (and, owing to the arbitrary nature of $\overset{*}{\boldsymbol{\varphi}}{}^{(1)^h}$, will ultimately be argued to be arbitrary). Using the isoparametric interpolation scheme, one also has:

$$\boldsymbol{X}^{h^e}(\boldsymbol{\eta}) = \sum_{a=1}^{n_{nes}} N_a(\boldsymbol{\eta}) \boldsymbol{X}_a. \tag{2.5}$$

Analogues of (2.3)–(2.5) are assumed to hold for body (2); i.e.

$$\begin{aligned} \boldsymbol{\varphi}^{(2)^{h\,e}}(\boldsymbol{\xi}) &= \sum_{b=1}^{n_{nes}} N_b(\boldsymbol{\xi}) \boldsymbol{d}_b^{(2)}(t), \\ \overset{*}{\boldsymbol{\varphi}}{}^{(2)^{h\,e}}(\boldsymbol{\xi}) &= \sum_{b=1}^{n_{nes}} N_b(\boldsymbol{\xi}) \boldsymbol{c}_b^{(2)}, \end{aligned} \tag{2.6}$$

and

$$\boldsymbol{Y}^{h^e}(\boldsymbol{\xi}) = \sum_{b=1}^{n_{nes}} N_b(\boldsymbol{\xi}) \boldsymbol{Y}_b, \tag{2.7}$$

defined over element surface parent domains $\mathcal{A}^{(2)^e}$.

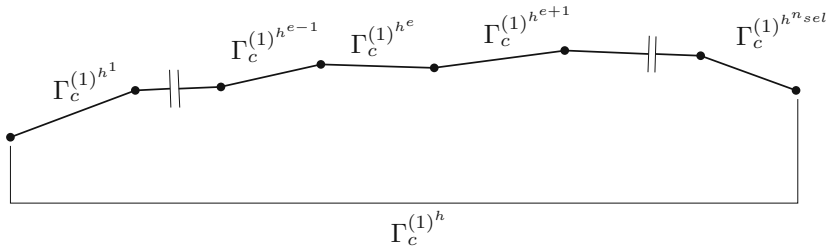

Figure 1. Division of the contact integral into subintegrals.

The contact virtual work in the discrete setting is now written, by substitution of the above discrete fields into (1.20), as

$$G^c(\boldsymbol{\varphi}_t^h, \overset{*}{\boldsymbol{\varphi}}{}^h) = \int_{\Gamma_c^{(1)^h}} [t_{N_t}^h \delta g^h + t_{T_{\alpha_t}}^h \delta \bar{\xi}^{\alpha^h}] \, d\Gamma, \tag{2.8}$$

where all quantities in the integrand depend on the discrete fields as given previously for the continuous case. As before, indices α, β, γ, etc. run between 1 and $n_{sd} - 1$ in (2.8) and in all other expressions in this chapter.

2.2 Numerical Integration of the Contact Integral

We now summarize the manner in which the contact virtual work integral is approximated in the traditional node-to-surface implementation. Dropping the subscript t's to reduce notation, (2.8) may be written as a sum of integrals over the n_{sel} element surfaces of $\Gamma_c^{(1)^h}$:

$$G^c(\boldsymbol{\varphi}^h, \overset{*}{\boldsymbol{\varphi}}{}^h) = \sum_{e=1}^{n_{sel}} \int_{\Gamma_c^{(1)^{h^e}}} [t_N^h \delta g^h + t_{T_\alpha}^h \delta \bar{\xi}^{\alpha^h}] \, d\Gamma. \tag{2.9}$$

where each subintegral of (2.9) is evaluated using quadrature. Figure 1 may be consulted for a graphic illustration of this division into subintegrals.

Performing a change of variables to the parent domain (i.e., $\mathcal{A}^{(1)^e}$) and applying an appropriate quadrature rule gives

$$\begin{aligned} G^c(\boldsymbol{\varphi}^h, \overset{*}{\boldsymbol{\varphi}}{}^h) &\approx \sum_{e=1}^{n_{sel}} \left\{ \sum_{k=1}^{n_{int}} W^k j(\boldsymbol{\eta}^k) [t_N^h(\boldsymbol{\eta}^k) \delta g^h(\boldsymbol{\eta}^k) + t_{T_\alpha}^h(\boldsymbol{\eta}^k) \delta \bar{\xi}^{\alpha^h}(\boldsymbol{\eta}^k)] \right\} \\ &= \sum_{e=1}^{n_{sel}} \left\{ \sum_{k=1}^{n_{int}} W^k j(\boldsymbol{\eta}^k) \delta \boldsymbol{\Phi}^{c^k} \cdot \boldsymbol{f}^{c^k} \right\} \end{aligned} \tag{2.10}$$

where n_{int} is the number of integration points per element surface of ${\Gamma_c^{(1)}}^h$ (corresponding to the quadrature rule in use), W^k is the quadrature weight corresponding to local quadrature point k, j is the jacobian of the transformation between the parent and reference domains, $\boldsymbol{\eta}^k \in {\mathcal{A}^{(1)}}^e$ is the (local) parent coordinate of quadrature point k, $\delta{\boldsymbol{\Phi}}^{c^k}$ is the vector of nodal variations corresponding to quadrature point k, and $\boldsymbol{f}^{c^k}$ is the (local) contact force vector, corresponding to quadrature point k. The quantities $\delta g^h(\boldsymbol{\eta}^k)$ and $\delta\bar{\xi}{\alpha}^h(\boldsymbol{\eta}^k)$ are computed using (1.14) and (1.15), with discrete fields replacing their continuous counterparts. The discrete contact virtual work is thus equal to a sum of individual quadrature point contributions. In particular, the global contact force vector $\boldsymbol{F}^c$ can be expressed as

$$\boldsymbol{F}^c = \mathop{\mathsf{A}}_{\tilde{k}=1}^{n_{sel}\cdot n_{int}} W^{\tilde{k}} j(\boldsymbol{\eta}^{\tilde{k}}) \boldsymbol{f}^{c^{\tilde{k}}} \tag{2.11}$$

where A is the standard finite element assembly operator and $\tilde{k}$ is a revised quadrature point index, which runs over all quadrature points in ${\Gamma_c^{(1)}}^h$.

The contact force contribution $\boldsymbol{f}^{c^{\tilde{k}}}$ from each quadrature point may be merely extracted from (2.10) once the vector of nodal variations for each quadrature point ($\delta{\boldsymbol{\Phi}}^{c^k}$) has been defined. To make the discussion more concrete with regard to $j(\boldsymbol{\eta}^k)$ and W^k, consider the case where nodal quadrature is employed to evaluate the element subintegrals generated by trilinear discretization in three dimensions (meaning each surface element is bilinearly interpolated). In this case the weights have the values $W^k = 1$, $k = 1 - 4$, and the $\boldsymbol{\eta}^k$'s are given by $\boldsymbol{\eta}^1 = (-1,-1)$, $\boldsymbol{\eta}^2 = (1,-1)$, $\boldsymbol{\eta}^3 = (1,1)$, and $\boldsymbol{\eta}^4 = (-1,1)$. At each point $\boldsymbol{\eta}^k$, the jacobian of the transformation is given by

$$j(\boldsymbol{\eta}^k) = \| {\boldsymbol{X}^{h^e}}_{,1}(\boldsymbol{\eta}^k) \times {\boldsymbol{X}^{h^e}}_{,2}(\boldsymbol{\eta}^k) \| \tag{2.12}$$

where the partial derivatives indicated in (2.12) are with respect to the surface coordinates η^1 and η^2 associated with ${\Gamma_c^{(1)}}^h$.

3 Mortar Formulation of Contact

Mortar methods were originally proposed as a technique for joining together potentially dissimilarly meshed domains (see, for example, Anagnostou et al. (1990). Several authors recognized the applicability of such methods to contact at an early stage, and proposed formulations for kinematically linear contact (see Belgacem et al. (1997); Hild (2000); McDevitt and Laursen (2000); El-Abbasi and Bathe (2001)). Here, we discuss the development of a mortar framework for large deformation problems, as summarized in a number of recent papers (see Puso and Laursen (2004a,b); Yang et al. (2005)). These have been shown to be robust for large deformation applications in both two and three dimensions, and under either dynamic or quasistatic circumstances.

In this section, we review some of the key constructs of mortar-based contact algorithms, by considering as a point of departure an alternative method for describing the virtual work expression in (2.8). In doing so, it is now more natural (in contrast to (2.8))

to represent the contact virtual work G^c in terms of *s*patial configuration quantities, via

$$G^c(\boldsymbol{\varphi}, \overset{*}{\boldsymbol{\varphi}}) = -\int_{\gamma_c^{(1)}} \boldsymbol{\lambda} \cdot \left(\overset{*}{\boldsymbol{\varphi}}^{(1)}(\boldsymbol{X}) - \overset{*}{\boldsymbol{\varphi}}^{(2)}(\bar{\boldsymbol{Y}}) \right) d\gamma, \tag{3.1}$$

where $\gamma_c^{(1)}$ is the current configuration of the (non-mortar) contact surface $\Gamma_c^{(1)}$, the mortar multiplier $\boldsymbol{\lambda}$ now denotes the Cauchy contact traction, and where $\boldsymbol{\varphi}^{(2)}(\bar{\boldsymbol{Y}})$ is the current position of the contact point for $\boldsymbol{X}$. Superscript h's have been omitted in (3.1) to simplify notation. As we have seen, in traditional contact implementations, the point $\bar{\boldsymbol{Y}}$ is typically explicitly determined for each point $\boldsymbol{X}$ at which which contact constraints are to be enforced. Here we will employ a spatial integration procedure which will only indirectly define pairings between points $\boldsymbol{X}$ and $\bar{\boldsymbol{Y}}$.

A discrete version of the contact problem is achieved through substitution of finite dimensional approximations for deformation mappings, variations, and Lagrange multipliers. This results in the following mortar approximation to the contact virtual work, denoted as G^{cm}:

$$G^{cm}(\boldsymbol{\varphi}^h, \overset{*}{\boldsymbol{\varphi}}^h) = -\sum_A^{ns} \sum_B^{ns} \sum_C^{nm} \boldsymbol{\lambda}_A \cdot \left[n_{AB}^{(1)} \overset{*}{\boldsymbol{\varphi}}_B^{(1)} - n_{AC}^{(2)} \overset{*}{\boldsymbol{\varphi}}_C^{(2)} \right]. \tag{3.2}$$

The expressions for $n_{AB}^{(1)}$ and $n_{AC}^{(2)}$ are key to the mortar formulation of contact, and involve inner products of surface shape functions:

$$\begin{aligned} n_{AB}^{(1)} &= \int_{\gamma^{(1)^h}} N_A^{(1)} \left(\xi^{(1)}(\boldsymbol{X}) \right) N_B^{(1)} \left(\xi^{(1)}(\boldsymbol{X}) \right) d\gamma, \\ n_{AC}^{(2)} &= \int_{\gamma^{(1)^h}} N_A^{(1)} \left(\xi^{(1)}(\boldsymbol{X}) \right) N_C^{(2)} \left(\xi^{(2)} \left(\bar{\boldsymbol{Y}}(\boldsymbol{X}) \right) \right) d\gamma. \end{aligned} \tag{3.3}$$

The normal and tangential portions of the contact operator are now exposed by splitting each nodal $\boldsymbol{\lambda}_A$ into normal and frictional parts:

$$\boldsymbol{\lambda}_A = \boldsymbol{\lambda}_{N_A} + \boldsymbol{\lambda}_{T_A}. \tag{3.4}$$

The normal part of the contact traction may be represented as (see Puso and Laursen (2004a))

$$\boldsymbol{\lambda}_{N_A} = -\lambda_{N_A} \boldsymbol{n}_A \text{ (no sum)} \tag{3.5}$$

where λ_{N_A} represents the contact pressure at node A. It is subject to Kuhn-Tucker conditions via

$$\begin{aligned} \lambda_{N_A} &\geq 0 \\ g_A &\leq 0 \\ \lambda_{N_A} g_A &= 0 \end{aligned} \tag{3.6}$$

where the mortar projected gap g_A at slave node A is defined as

$$\begin{aligned} g_A &= \boldsymbol{n}_A \cdot \boldsymbol{g}_A, \\ \boldsymbol{g}_A &= \kappa_A \left[\sum_B^{ns} n_{AB}^{(1)} \boldsymbol{\varphi}_B^{(1)} - \sum_C^{nm} n_{AC}^{(2)} \boldsymbol{\varphi}_C^{(2)} \right], \end{aligned} \tag{3.7}$$

where κ_A is a scale factor defined as

$$\begin{aligned} \kappa_A &= \frac{1}{\sum_D n_{AD}^{(1,ref)}}, \\ n_{AD}^{(1,ref)} &= \int_{\Gamma^{(1)^h}} N_A^{(1)}\left(\xi^{(1)}(\boldsymbol{X})\right) N_D^{(1)}\left(\xi^{(1)}(\boldsymbol{X})\right) d\Gamma. \end{aligned} \tag{3.8}$$

The scaling defined in (3.8), while not by any means unique, is performed so that the gap function $\boldsymbol{g}_A$ is dimensionally correct; this feature is of crucial importance when implementing penalty methods in particular. Equation (3.7) is written in terms of a nodal normal $\boldsymbol{n}_A$ associated with each slave node A.

Although other implementations of mortar-based frictional contact are possible, we consider here a penalty regularization of the Coulomb frictional conditions. This may be expressed via

$$\begin{aligned} \mathcal{L}_v \boldsymbol{\lambda}_T &= \epsilon_T \left[\boldsymbol{v}_T - \dot{\gamma} \frac{\boldsymbol{\lambda}_T}{\left\| \boldsymbol{\lambda}_T \right\|} \right] \\ \Phi := \left\| \boldsymbol{\lambda}_T \right\| - \mu \left\| \boldsymbol{\lambda}_N \right\| &\leq 0 \\ \dot{\gamma} &\geq 0 \\ \Phi \dot{\gamma} &= 0 \end{aligned} \tag{3.9}$$

where ϵ_T is the frictional penalty parameter. The frictional conditions in (1.23) are recovered in the limit as $\epsilon_T \to \infty$. $\mathcal{L}_v \boldsymbol{\lambda}_T$ is the *Li*e derivative of the frictional traction, giving rise (for example) to the sort of expression for the slip rate given previously in (1.19). Note that (1.19) contains material time derivatives of the components of $\boldsymbol{\lambda}_T$ only; the absence of derivatives of base vectors assures its frame indifference.

As shown in Yang et al. (2005), the notion of frame indifferent slip velocity needs to be adapted somewhat when one moves from the node-to-surface to mortar framework for contact analysis. An appropriate notion of tangential velocity to use in a mortar projected framework is

$$\boldsymbol{v}_{T_A} = -\kappa_A \left[\sum_C^{nm} \dot{n}_{AC}^{(2)} \boldsymbol{\varphi}_C^{(2)} - \sum_B^{ns} \dot{n}_{AB}^{(1)} \boldsymbol{\varphi}_B^{(1)} \right] \cdot (\boldsymbol{I} - \boldsymbol{n} \otimes \boldsymbol{n}) \tag{3.10}$$

where $\dot{n}_{AC}^{(2)}$ and $\dot{n}_{AB}^{(1)}$ are time derivatives of the mortar integrals (holding node A constant). Note that the scaling factors κ_A have again been introduced to retain dimensional consistency. Since the mortar integral time derivatives are invariant with respect to any rigid body motion relative to the original spatial frame, $\boldsymbol{v}_{T_A}$ is frame indifferent.

With these definitions in hand, a trial state-return map strategy is employed to determine the Coulomb frictional tractions in an algorithmic, time stepping procedure. The

algorithm begins by computation of a trial state, assuming no slip during the increment:

$$\begin{aligned}\boldsymbol{\lambda}^{trial}_{T_{A_{n+1}}} = \boldsymbol{\lambda}_{T_{A_n}} - \epsilon_T \kappa_A \Bigg[\sum_{C}^{nm} \left(n^{(2)}_{AC_{n+1}} - n^{(2)}_{AC_n} \right) \boldsymbol{\varphi}^{(2)}_C \\ - \sum_{B}^{ns} \left(n^{(1)}_{AB_{n+1}} - n^{(1)}_{AB_n} \right) \boldsymbol{\varphi}^{(1)}_B \Bigg] \cdot (\boldsymbol{I} - \boldsymbol{n}_A \otimes \boldsymbol{n}_A),\end{aligned} \tag{3.11}$$

with a corresponding trial value for the slip function

$$\Phi^{trial}_{A_{n+1}} = \left\| \boldsymbol{\lambda}^{trial}_{T_{A_{n+1}}} \right\| - \mu |\lambda_{N_{A_n}}|. \tag{3.12}$$

A return map is then used to define the final frictional traction via

$$\boldsymbol{\lambda}_{T_{A_{n+1}}} = \begin{cases} \boldsymbol{\lambda}^{trial}_{T_{A_{n+1}}} & \text{if } \Phi^{trial}_{A_{n+1}} \leq 0 \text{ (stick)}, \\ \mu |\lambda_{N_{A_n}}| \frac{\boldsymbol{\lambda}^{trial}_{T_{A_{n+1}}}}{\| \boldsymbol{\lambda}^{trial}_{T_{A_{n+1}}} \|} & \text{otherwise (slip)}. \end{cases} \tag{3.13}$$

In these expressions, the subscript $n+1$ means a state associated with the current iteration for the unknown solution at t_{n+1}, while n is associated with the last (converged) time level.

4 Numerical Examples of Mortar Contact Treatment

A few numerical examples are now given to demonstrate the accuracy and robustness of the mortar contact approach.

4.1 Hertzian Contact

A cylinder on cylinder Hertzian contact problem is presented first to investigate the accuracy characteristics of this formulation (see Figure 2). The cylinders are modelled as consistent of isotropic linear elastic materials ($E = 200.0$, $\nu = 0.3$), and the Coulomb friction coefficient is taken as 0.2.

The cylinders are pressed together by a distributed pressure p, inducing a normal contact force P at the point of contact. Subsequently, a second distributed load q is applied in the tangential direction of the plane. The finite element meshes are shown in Figure 3; while the comparison of the numerical result and the analytical solution Johnson (1985) for the surface tractions is given in Figure 4. There are some small differences between the solutions because we use a large deformation formulation; furthermore, some spatial oscillations in the numerical solution for the frictional traction are present, seemingly due to the nonsmoothness of the frictional traction field at the stick slip boundary. Notably, these oscillations disappear for fine meshes (see Figure 5).

4.2 Three Dimensional Torus–Cylinder Impact Example

A three dimensional problem now serves to demonstrate the performance of the approach in a truly large deformation application. The initial configuration and the finite

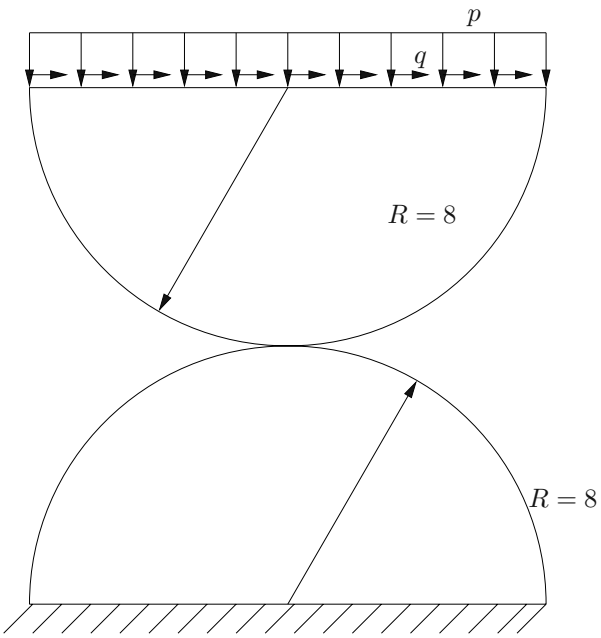

Figure 2. Schematic of the cylinder on cylinder Hertzian contact problem.

element mesh for this example are given in Figure 6; in this problem, the torus will be given an initial velocity such that it actually penetrates and moves through the cylinder. The torus and the cylinder are idealized as Neo-Hookean hyperelastic materials, with $E = 2250$ and $\nu = 0.3$.; the reference density of the two bodies is $\rho = 0.1$. Frictionless response is assumed in the bodies between the two bodies. The deformed configurations at different time steps are shown in Figure 7. Table 1 shows the superior convergence performance (with tolerance 1×10^{-18}) of the mortar contact method for this problem, using Newton-Raphson iteration on the global nonlinear equations.

4.3 A three dimensional postbuckling problem

This example demonstrates the performance of the algorithm for three dimensional self-contact problems. Self-contact can happen in a postbuckling process such as a car crash. In this example, we analyze a cylinder postbuckling problem. The initial configuration and the finite element mesh are given in Figure 8. The bottom surface of the cylinder is fixed and a vertical displacement is applied on the top surface. Figure 9 shows a sequence of buckling modes. Note that only half of the cylinder is plotted to see the deformation more clearly. The height of the cylinder is 50 mm, the diameter is 15 mm, and the thickness is 0.5 mm. The cylinder is made of aluminum and is discretized with 1800 eight-node finite strain elastoplastic elements, and the material properties are bulk

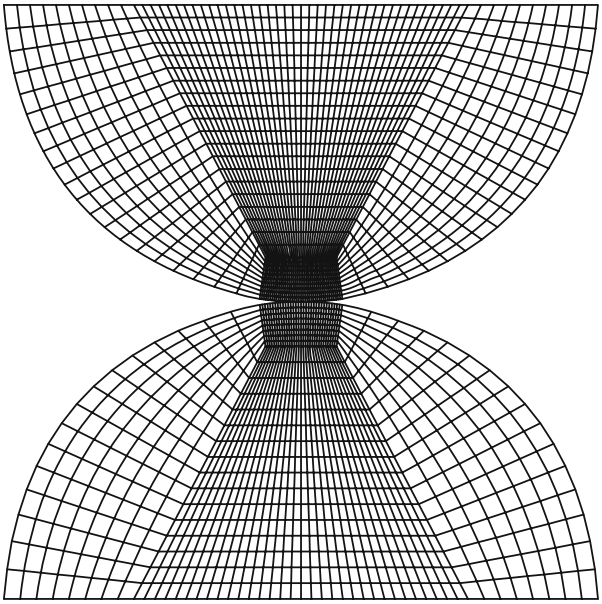

Figure 3. Mesh for the Hertzian contact problem.

modulus $K = 63.84$ GPa, shear modulus $G = 26.12$ GPa, yield stress $\sigma_Y = 31$ MPa, and a linear hardening rate $H = \frac{G}{100}$. Two self-contact surfaces are predefined, i.e., the inner and outer surfaces of the cylinder (we preclude the possibility of contact between inner and outer surfaces). We ignore the friction traction on the two self-contact surfaces (there is only a small amount of sliding). The applied displacement on the top of the cylinder is $\boldsymbol{d} = \begin{bmatrix} 0.0 & 0.0 & 60.0t \end{bmatrix}^T$, where t is the load factor.

Figure 10 shows the curve of the reaction force vs. displacement at the top with a sequence of buckle cycles in the curve. The contribution of self-contact is clearly shown. It is this contact, manifested in the figure as a reversal of load at the bottom of each buckle cycle, which provides the stiffening mechanism necessary to trigger the next buckle.

This problem is extremely nonlinear because the deformation also induces large plastic strains in the cylinder. Table 2 presents the Newton-Raphson convergence sequences at two different load steps with different load increments. When $d = 24$ mm and $\triangle d = 0.3$ mm, it struggles at the first few iterations and finally converged quadratically with the help of line searches. All other cases presented in the table converge quadratically without using line search.

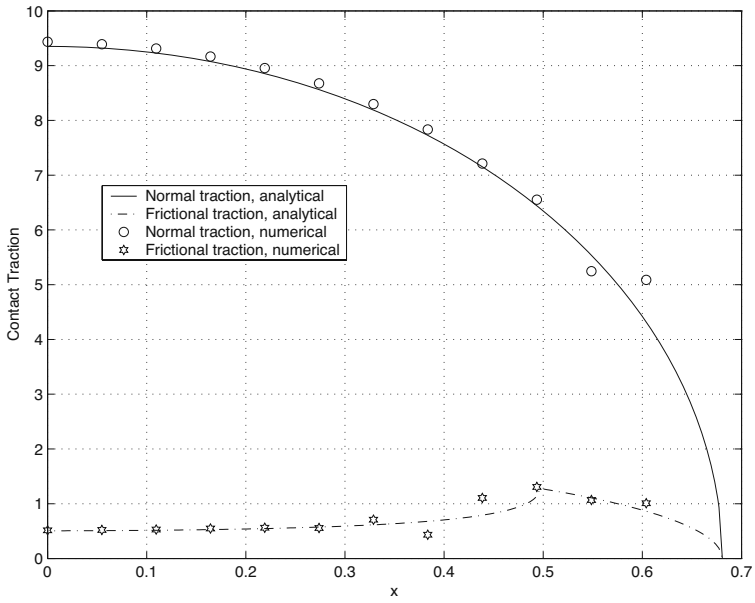

Figure 4. Computed nodal contact tractions for frictional cylinder on cylinder contact problem; coarse mesh.

4.4 A Three Dimensional Flat Tire Rolling Problem

A highly loaded rolling tire is analyzed in this problem to further test the efficiency and robustness of the proposed self-contact algorithm. In this example, the inner tire surfaces undergo self-contact, requiring a high degree of robustness of the searching algorithm and in the contact formulation. The diameter of the tire wheel is 16 inches, the width of the tire is 235 mm, and the height of the tire is 806 mm. A neo-Hookean hyperelastic material model is assumed, with an initial Young's modulus of $E = 2250$ MPa and Poisson's ratio $\nu = 0.45$. The frictional coefficients for the contact between tire and the road surface and for the contact inside the tire are both chosen to be 0.5. The initial configuration and the finite element mesh is given in Figure 11. A vertical loading (displacement controlled) is first applied to deform the tire until self-contacts occur and contact pressure reaches a certain level. The tire is then rolled and displacements are applied on the tire wheel surface. Inertial effects are ignored and the road is considered to be rigid. Deformed configurations at different load steps are shown in Figure 12, where (c) and (d) only show a quarter of the tire to demonstrate self-contact inside the tire and the rotation of the tire. As the figure indicates, significant deformation, as well as sliding, occur in this problem. This example further demonstrates the applicability of the proposed techniques to very challenging contact and self-contact problems. Table 3 presents the quadratic

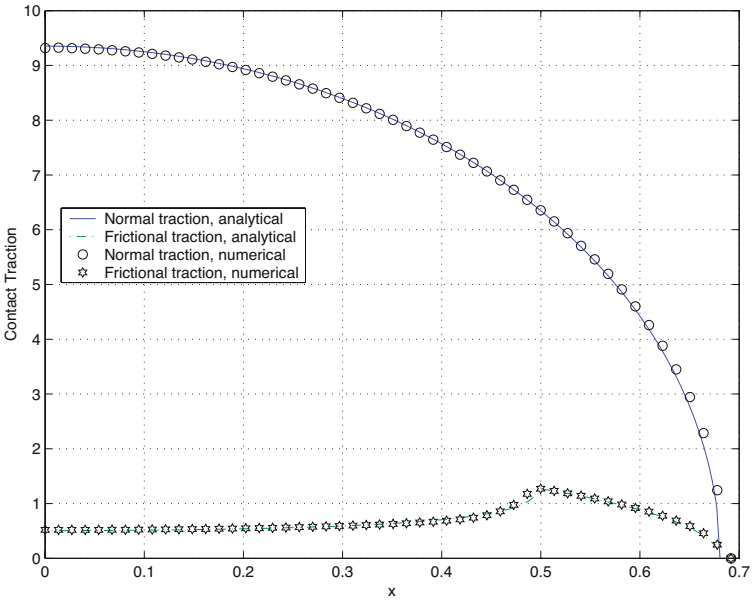

Figure 5. Computed nodal contact tractions for frictional cylinder on cylinder contact problem; finer mesh.

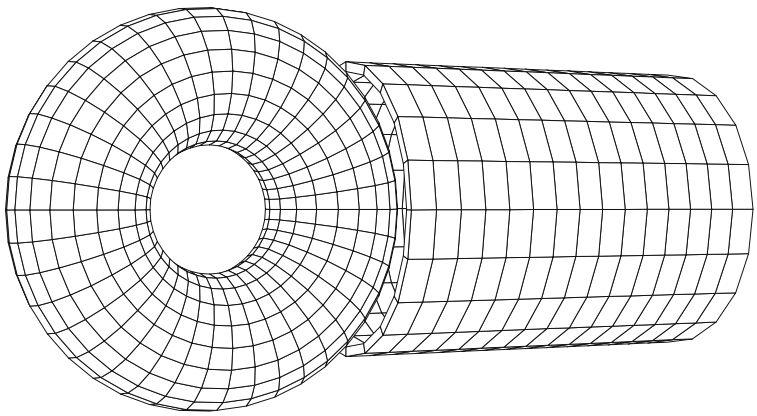

Figure 6. The initial configuration of the torus cylinder impact problem.

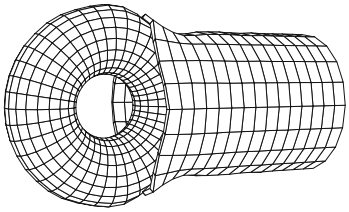

(a)

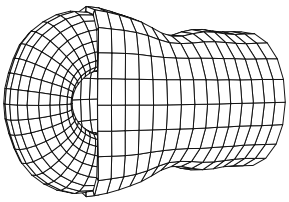

(b)

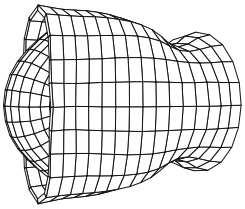

(c)

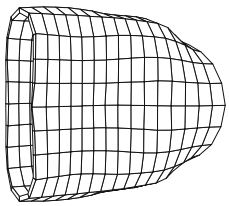

(d)

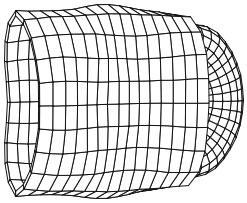

(e)

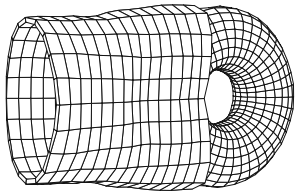

(f)

Figure 7. Deformed configurations of the torus–cylinder impact problem: (a) $t = 1$; (b) $t = 2.5$; (c) $t = 4.0$; (d) $t = 5.5$; (e) $t = 7.0$; (f) $t = 8.5$.

Table 1. Energy norms of convergence sequences at different time steps; torus-cylinder impact problem.

Iteratons	$t = 1$	$t = 4$	$t = 6$	$t = 8$
1	1.78E-08	1.20E-05	9.23E-04	3.22E-06
2	4.49E-19	3.78E-12	1.05E-08	3.82E-14
3		1.53E-23	1.50E-17	6.01E-29
4			2.64E-28	

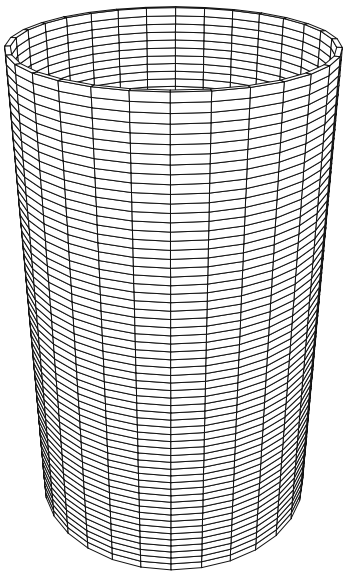

Figure 8. The initial configuration of the cylinder postbuckling problem.

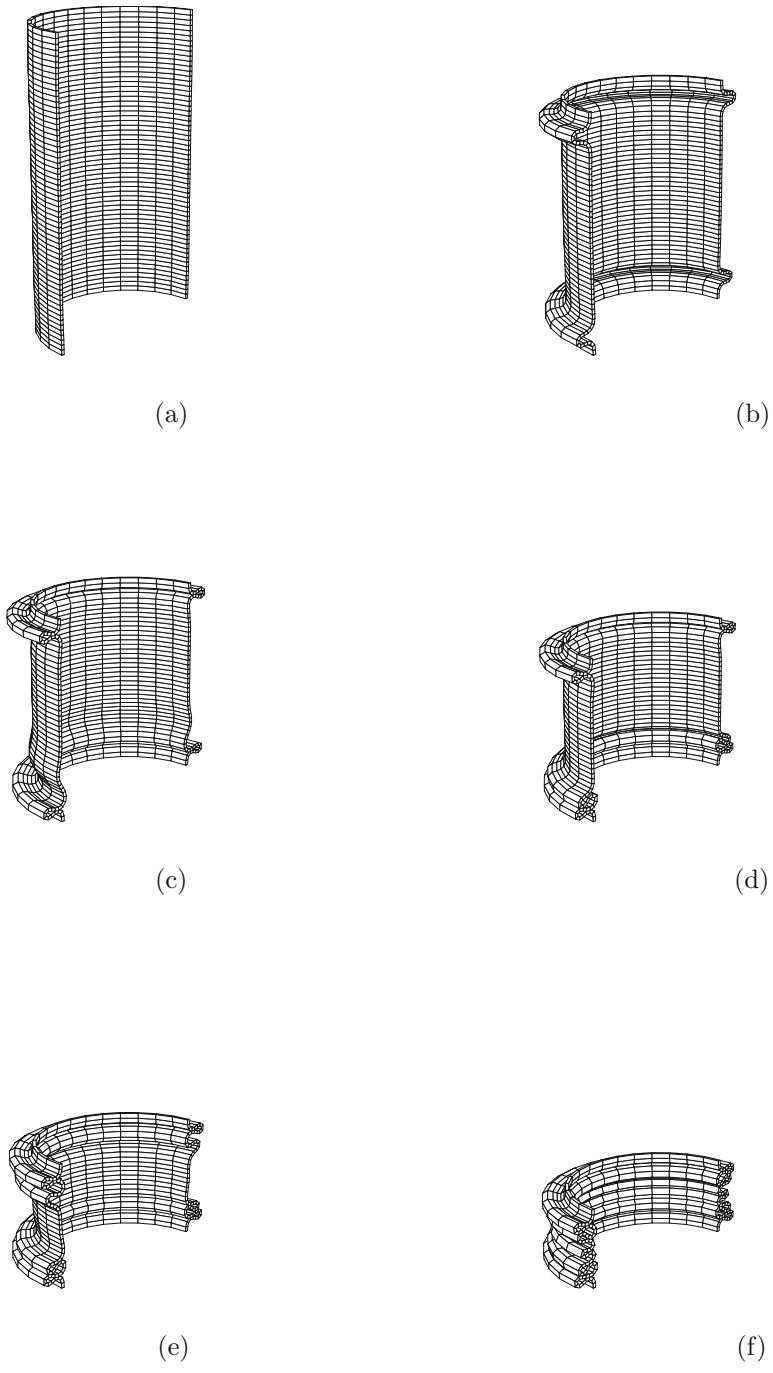

Figure 9. Deformed configurations of the cylinder post-buckling problem at different time steps.